






# Peculiar Orbital Characteristics of Earth Quasi-Satellite 469219 Kamo‘oalewa: Implications for the Yarkovsky Detection and Orbital Uncertainty Propagation

Shoucun Hu<sup>1,2,3</sup> , Bin Li<sup>1,2,3</sup>, Haoxuan Jiang<sup>1</sup> , Gang Bao<sup>1</sup>, and Jianghui Ji<sup>1,2,3</sup> 

<sup>1</sup> CAS Key Laboratory of Planetary Sciences, Purple Mountain Observatory, Chinese Academy of Sciences, Nanjing 210023, People’s Republic of China; [hushoucun@pmo.ac.cn](mailto:hushoucun@pmo.ac.cn), [jijh@pmo.ac.cn](mailto:jijh@pmo.ac.cn)

<sup>2</sup> CAS Center for Excellence in Comparative Planetology, Hefei 230026, People’s Republic of China

<sup>3</sup> School of Astronomy and Space Science, University of Science and Technology of China, Hefei 230026, People’s Republic of China

Received 2023 April 29; revised 2023 August 1; accepted 2023 August 26; published 2023 September 29

## Abstract

469219 Kamo‘oalewa is selected as one of the primary targets of Tianwen-2 mission, which is currently believed to be the most stable quasi-satellite of Earth. Here we derive a weak detection of the Yarkovsky effect for Kamo‘oalewa, giving  $A_2 = (-1.075 \pm 0.447) \times 10^{-13}$  au day<sup>-2</sup>, with the available ground-based optical observations from Minor Planet Center and a relatively conservative weighting scheme. Due to the quasi-satellite resonance with Earth, we show that the detection of the Yarkovsky effect by orbital fitting with astrometric observations becomes difficult, as its orbital drift shows a slow oscillatory growth resulting from the Yarkovsky effect. In addition, we extensively explore the characteristics of orbital uncertainty propagation and find that the positional uncertainty mainly arises from the geocentric radial direction in 2010–2020 and then concentrates in the heliocentric transverse direction in 2020–2030. Furthermore, the heliocentric transverse uncertainty is clearly monthly dependent, which can arrive at a minimum around January and a maximum around July as the orbit moves toward the leading and trailing edges, respectively, in 2025–2027. Finally, we investigate a long-term uncertainty propagation in the quasi-satellite regime, implying that the quasi-satellite resonance with Earth may play a crucial role in constraining the increase of uncertainty over time. Such an interesting feature further implies that the orbital precision of Kamo‘oalewa is relatively stable at its quasi-satellite phase, which may also be true for other quasi-satellites of Earth.

*Unified Astronomy Thesaurus concepts:* Asteroids (72); Asteroid dynamics (2210)

## 1. Introduction

Near-Earth asteroids are defined as those with perihelion distances less than 1.3 au. Among them, there is a special classification called Earth co-orbital asteroids that are captured in a 1:1 mean motion resonance with Earth (Namouni 1999). Such asteroids have three typical orbital configurations, i.e., tadpole orbit that moves about the Lagrangian points L4 and L5, horseshoe orbit librating with a large amplitude (as large as to around 180°) in longitude in the frame corotating with Earth, and quasi-satellite orbit librating around 0° (typically with small amplitudes; Connors et al. 2002; Morais & Morbidelli 2002). Under the influence of a complex gravitational environment, the orbits may periodically switch between horseshoe and quasi-satellite configurations (Sidorenko et al. 2014; Qi & Qiao 2022).

469219 Kamo‘oalewa (provisional designation is 2016 HO3) is a fast-rotating near-Earth asteroid discovered by the Pan-STARRS1 survey telescope at the Haleakala Observatory in Hawaii on 2016 April 27 (De la Fuente Marcos & De la Fuente Marcos 2016; Tholen et al. 2016). The asteroid has a quasi-satellite orbit with respect to Earth, with a semimajor axis of 1.001 au, an eccentricity of 0.103, and an orbital inclination of 7°79'. Spectral observations indicate that Kamo‘oalewa may comprise lunar material, and the albedos ranging from 0.10 to 0.16 give an estimate of the effective diameter of 58–46 m (Sharkey et al. 2021; Winter et al. 2022). The amplitudes of

light curves suggest that the shape of this object is probably elongated, with a length-to-width ratio of less than 0.48 (Li & Scheeres 2021). The spin period of Kamo‘oalewa is  $28.3_{-1.3}^{+1.8}$  minutes (Sharkey et al. 2021), which is lower than the critical value of  $\sim 2.2$  hr (Pravec & Harris 2000), implying that internal cohesion is required to maintain its internal structure (Hu et al. 2021; Li & Scheeres 2021).

The orbit of Kamo‘oalewa exhibits both retrograde and prograde motions in the geocentric inertial frame, while it turns entirely retrograde in the geocentric corotating frame (Pousse et al. 2017) as shown in Figure 1. Orbital propagation shows that its quasi-satellite state remains very stable, with a geocentric distance oscillating in the range 0.1–0.3 au (outside Earth’s Hill radius 0.01 au). Long-term simulations show that its orbit periodically switches between horseshoe and quasi-satellite configurations, and its current orbit state began about 100 yr ago and will transition back to the horseshoe orbit in roughly 300 yr (De la Fuente Marcos & De la Fuente Marcos 2016; Sharkey et al. 2021). Kamo‘oalewa is a good target for low-cost in situ study (Heiligers et al. 2019; Venigalla et al. 2019) owing to its peculiar orbit relative to Earth. In addition, the China National Space Administration (CNSA) will launch a sample-return mission to this asteroid around 2025 (Chi et al. 2018; Huang et al. 2020; Zhang et al. 2021a, 2021b), which will be the second mission of China to closely rendezvous a near-Earth asteroid (Huang et al. 2013). Numerical simulations with ground-based and onboard radio-metric tracking data were performed to estimate the GM value, which is a major challenge owing to the tiny mass of the asteroid (Jin et al. 2020; Yan et al. 2022).

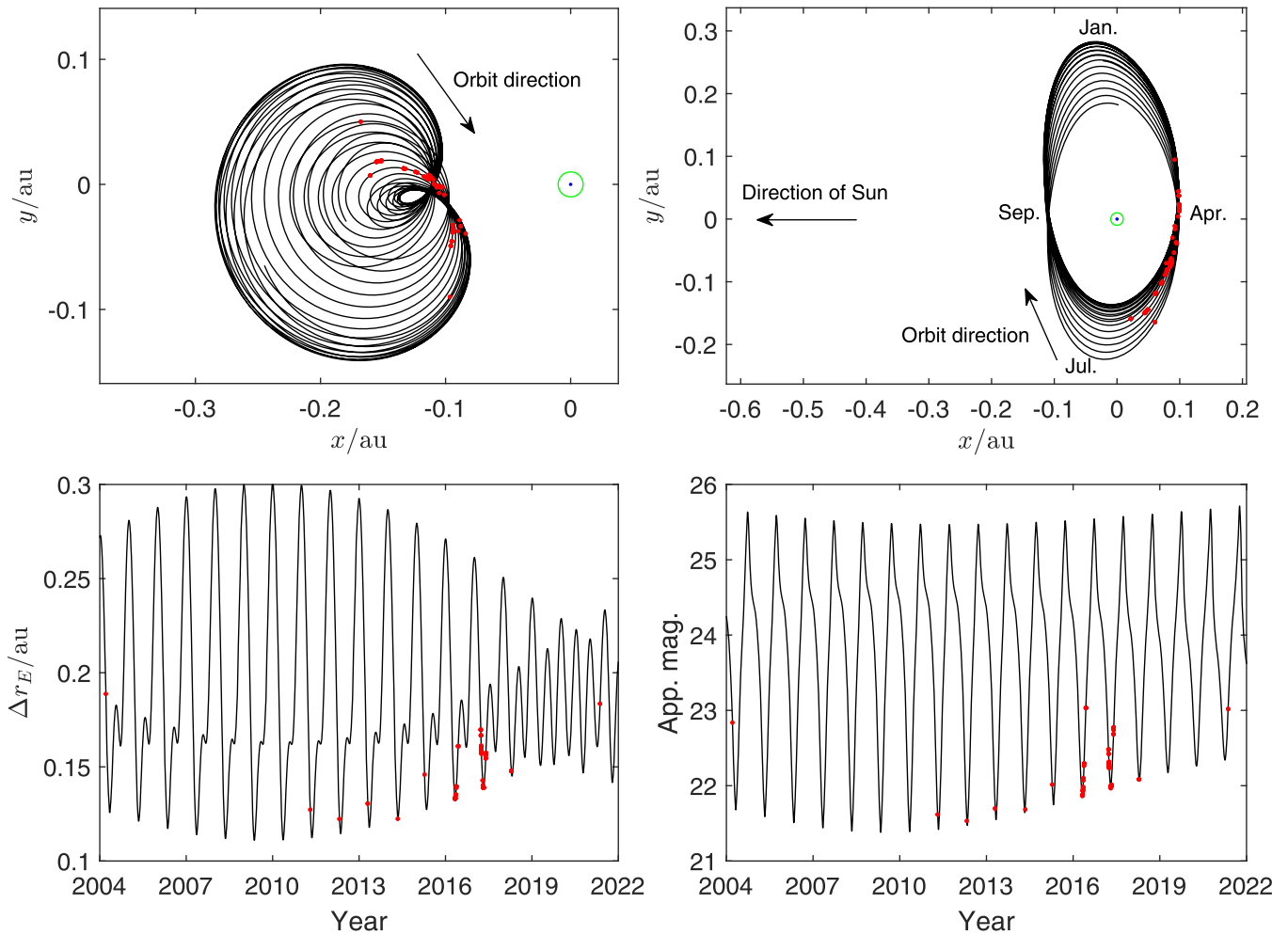


**Figure 1.** The top panels show the geocentric orbit of Kamo'oailewa in the mean ecliptic reference frame of J2000.0 and the Sun–Earth rotating frame, respectively (both are projected from the direction of the north ecliptic pole). The bottom panels show the variations in the geocentric distance and apparent magnitude, respectively. The time span ranges from 2004 to 2022. The red circles mark up the observation epochs, while the green circles represent Earth's Hill sphere.

The Yarkovsky effect is a radiation recoil force acting on rotating asteroids caused by anisotropic thermal emission of absorbed sunlight (Vokrouhlický et al. 2000), which plays a fundamental role as a nongravitational force in the orbital evolution of near-Earth asteroids, especially for smaller objects (Bottke et al. 2002; Morbidelli & Vokrouhlický 2003; Bottke et al. 2006). The transverse component of Yarkovsky acceleration gives rise to a typically slow variation in the semimajor axis, as well as a long-term drift in the mean anomaly (Farinella et al. 1998). Long-term dynamical simulations that included the Yarkovsky effect suggest that the mechanism can cause an earlier removal of the asteroid from current co-orbital configuration than that of a gravity-only model does (Fenucci & Novaković 2021).

The Yarkovsky acceleration can vary as a function of mass, spin state, and surface thermal properties (Vokrouhlický 1999). Direct calculation of the force by thermophysical modeling is usually unrealistic owing to the unknown parameters for a vast majority of near-Earth asteroids. The effect for a 1 km sized object generally results in a subtle drift of  $\sim 10^{-3}$  au Myr $^{-1}$  in the semimajor axis, with a related magnitude of acceleration close to the order of gravitational perturbation from the main belt (Nugent et al. 2012). If accurate radar observations are available or optical observations cover a long arc, this effect can be detected from orbital fitting (Nugent et al. 2012;

Farnocchia et al. 2013; Deo & Kushvah 2017; Greenberg et al. 2017; Del Vigna et al. 2018; Liu et al. 2022). Greenberg et al. (2020) presented the detection of the Yarkovsky effect for 247 near-Earth asteroids with optical and radar astrometry, and high-precision observations will reveal substantial detections (Chesley et al. 2016; Desmars 2015; Dziadura et al. 2022). If the shape, diameter, and spin state of the asteroid are measured from mid-IR observations, the bulk density and even the thermophysical properties such as thermal inertia may be further unveiled by the Yarkovsky drift (Chesley et al. 2003; Rozitis & Green 2011; Rozitis et al. 2013; Chesley et al. 2014; Rozitis & Green 2014; Hanuš et al. 2018; Jiang et al. 2019; Fenucci et al. 2021).

Recently, Liu et al. (2022) presented the Yarkovsky detection for Kamo'oailewa using a modified open-source software. Here we aim to perform a comprehensive study of the Yarkovsky detection and understand orbital uncertainty propagation characteristics for Kamo'oailewa. In addition, we employ our developed orbital determination package that adopts a slightly more conservative consideration of the weighting scheme to conduct orbital fitting, resulting in a weak detection of Yarkovsky drift of the asteroid. Based on a series of orbital determination simulations, we further show that Kamo'oailewa's peculiar quasi-satellite orbit makes it difficult to detect the Yarkovsky effect with ground-based

optical observations. We then study the characteristics of the orbital uncertainty in the next few years to provide information for the Tianwen-2 mission. Furthermore, we find that the uncertainty propagation of Kamoʻoalewa in the quasi-satellite regime can be constrained by the quasi-satellite resonance with Earth, which is an interesting feature for such a stable quasi-satellite.

The paper is structured as follows. Section 2 describes the adopted observations for orbital fitting, along with the dynamical model and detection method of the Yarkovsky effect. In Section 3, we show the orbital behavior of Kamoʻoalewa involved in the Yarkovsky effect and derive a weak detection of the Yarkovsky effect from the fitting. In Section 4, we explore the characteristics of orbital uncertainty with given orbital solutions and carry out a secular investigation in the quasi-satellite regime. Finally, we summarize the main results in Section 5.

## 2. Observations and Models

### 2.1. Ground-based Optical Astrometry

Considering the small size and relatively large geocentric distance ( $\Delta r_E$ ) of Kamoʻoalewa, ground-based radar observations are unavailable. However, its stable orbit with respect to Earth allows it to have a good observational window around April once a year. As of 2022 November 1, 310 measurements of R.A. and decl. spanning from 2004 March 17 to 2021 May 13 were released from 10 different observatories at MPC, among which the observations by station T12 (University of Hawaii 2.24 m telescope, Maunakea) contribute a large portion of 70%. Figure 1 shows the orbit in the geocentric ecliptic frame, geocentric rotating frame, time evolution of  $\Delta r_E$ , and apparent magnitude from 2004 to 2022, where the red circles correspond to the observation epochs (see also De la Fuente Marcos & De la Fuente Marcos 2016).

### 2.2. Yarkovsky Modeling

The Yarkovsky effect can be an important source of uncertainty in the orbit propagation of a near-Earth asteroid (Chesley et al. 2014). Generally, only the transverse component of the force needs to be considered in the modeling. The following simple expression is adopted to quantify the force (Del Vigna et al. 2018):

$$\mathbf{F}_{\text{Yar}} = A_2 \left( \frac{r_0}{r} \right)^d \hat{\mathbf{t}}, \quad 0.5 \leq d \leq 3.5, \quad (1)$$

where  $r_0 = 1$  au and  $d$  is a parameter related to the thermo-physical properties. Here  $d = 2$  is assumed, though its specific value has little effect on the orbit since the heliocentric distance  $r$  of Kamoʻoalewa is always around 1 au. Parameter  $\hat{\mathbf{t}}$  is a unit vector pointing to the transverse direction of the orbit, and  $A_2$  is a free parameter, reflecting the strength of the Yarkovsky acceleration. The mean semimajor axis drift rate can then be expressed as (Farnocchia et al. 2013)

$$\langle da/dt \rangle = \frac{2A_2(1 - e^2)}{n} \left( \frac{r_0}{p} \right)^2, \quad (2)$$

where  $a$ ,  $e$ , and  $n$  denote the semimajor axis, the eccentricity, and the mean motion, respectively, and  $p$  is the semilatus rectum  $a(1 - e^2)$ .

### 2.3. Dynamical Model

To detect the Yarkovsky effect, a high-fidelity dynamical force model is required to compute the orbit. Here the Newtonian accelerations of the Sun (as well as the relativistic effect), the eight major planets, the Moon, and the 16 massive main-belt asteroids are considered (Farnocchia et al. 2013), using the JPL planetary ephemeris DE440 to calculate the positions of the planets during the orbital computation (Park et al. 2021). Since the orbit is limited to around 1 au, the uncertainty caused by other massive asteroids is negligible at the current accuracy. In addition, the oblateness perturbation of the Sun and Earth, as well as the solar radiation pressure, can also be safely ignored at the current level of observation accuracy (Liu et al. 2022).

### 2.4. Method of Yarkovsky Effect Detection

In this work, we perform the orbital fitting with a seven-dimensional differential correction in both the orbital elements and  $A_2$  simultaneously from the data set (Farnocchia et al. 2013). Here we have developed a software called the Small-Body ORbit Determination package (SBORD) to perform orbital determination with ground-based optical astrometry. A weighted least-squares algorithm is adopted to fit the astrometric measurements (Milani & Gronchi 2010). The latest debiasing technique by Eggl et al. (2020) and the weighting scheme by Vereš et al. (2017) are implemented to process the data. The outlier rejection scheme adopted is the same as Greenberg et al. (2020). The Runge–Kutta–Fehlberg (RKF78) method is used to propagate the orbit of the asteroid (Fehlberg 1969).

To examine the reliability of SBORD, we perform an orbital fit for the near-Earth asteroid (499998) 2011 PT with the observations from 2011 to 2017 given by MPC. Next, we measure the Yarkovsky drift of  $A_2 = (-2.133 \pm 0.296) \times 10^{-13}$  au day $^{-2}$  for 2011 PT (the epoch is 2023 February 25 TDB), which agrees well with the JPL Horizons solution of  $A_2 = (-2.121 \pm 0.301) \times 10^{-13}$  au day $^{-2}$  and the NEODYs-2 solution of  $A_2 = (-2.241 \pm 0.298) \times 10^{-13}$  au day $^{-2}$ . As indicated subsequently, we will compare our gravity-only solution of Kamoʻoalewa with that of the JPL Horizons system.

The reliability of the Yarkovsky detection depends strongly on the orbital arc and the quality of the observations. The signal-to-noise ratio  $S/N = |\langle da/dt \rangle / \sigma_{\langle da/dt \rangle}| = |A_2 / \sigma_{A_2}|$  is commonly used to estimate the significance (Farnocchia et al. 2013): the detections that satisfy  $S/N \geq 3$  and  $S \leq 2$  are accepted as valid detections (Chesley et al. 2016; Del Vigna et al. 2018), where

$$S = \left| \frac{\langle da/dt \rangle}{\langle da/dt \rangle_{\text{exp}}} \right| \quad (3)$$

is an indicator parameter used to assess whether the derived drift  $\langle da/dt \rangle$  is physically possible and  $\langle da/dt \rangle_{\text{exp}}$  is the expected value that can be estimated by scaling the parameters of Bennu (Del Vigna et al. 2018).

## 3. Analysis of Orbital Fit

### 3.1. Orbital Characteristics

To better understand the detection of the Yarkovsky effect, the orbital characteristics of Kamoʻoalewa should be

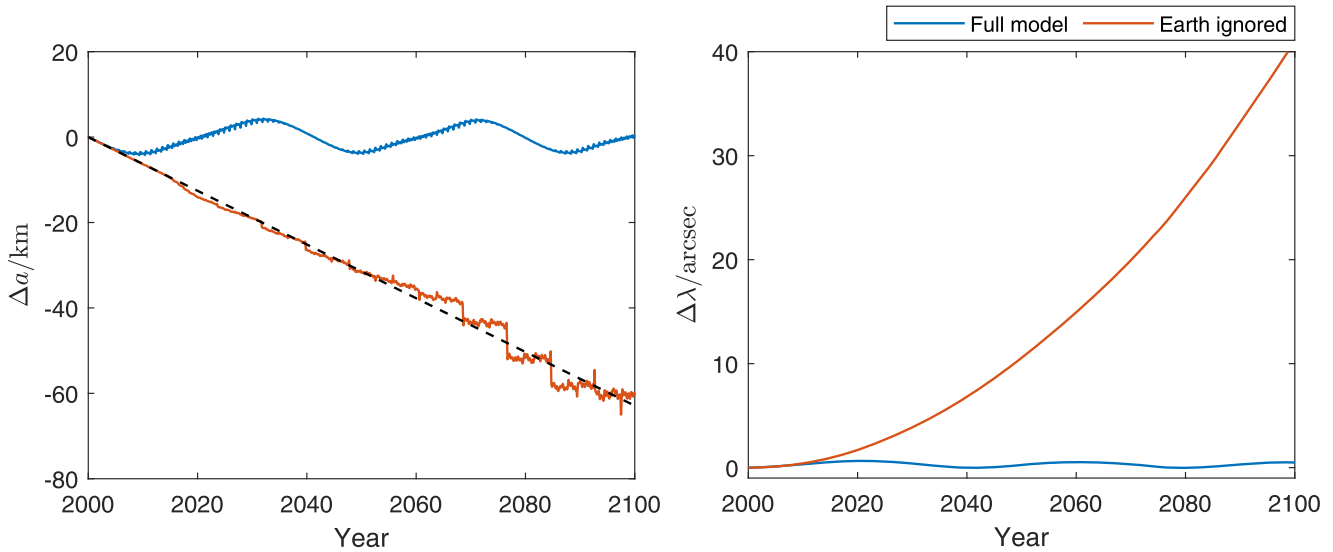


**Figure 2.** The two panels show the changes in  $\Delta a$  and  $\Delta \lambda$  for Kamo'oailewa from 2000 to 2100 with the same initial states.  $\Delta a$  and  $\Delta \lambda$  are the differences of the semimajor axis and the mean longitude between the Yarkovsky-included and the gravity-only models. The difference between the blue lines and the red lines is that the former includes all the planetary gravitational perturbations while the latter includes all of those but Earth. The black dashed line is the  $\Delta a$  computed with the analytical method (Equation (2)). The value of  $A_2$  in these figures is assumed to be  $-1.0 \times 10^{-13}$  au day $^{-2}$ .

investigated. As mentioned by Sharkey et al. (2021), the semimajor axis exhibits periodical oscillations with a longer period of  $\sim 40$  yr owing to the quasi-satellite resonance with Earth. For a better measurement of the Yarkovsky effect, a larger orbital drift over time under the influence of the Yarkovsky effect is preferred.

The two panels in Figure 2 show the time evolution of the differences in the semimajor axis and the mean longitude (denoted as  $\Delta a$  and  $\Delta \lambda$ , respectively) between the Yarkovsky-included and gravity-only models with the same initial states from 2000 to 2100 for an assumed value of  $A_2 = -1.0 \times 10^{-13}$  au day $^{-2}$ . Two scenarios are considered in Figure 2, where one includes the full planetary gravitational perturbations (as described in Section 2.3), whereas the other model considers all of the perturbation except the gravity of Earth. Figure 2 exhibits that when Earth's orbital perturbation is excluded, the drifts in the semimajor axis and the mean longitude caused by the Yarkovsky effect are shown to vary linearly and quadratically with time, respectively. Moreover, the difference of the semimajor axis  $\Delta a$  is in good agreement with that predicted by the analytical method (Equation (2)). In this situation, Kamo'oailewa would not move in the quasi-satellite orbit but behave like a normal asteroid beyond the mean motion resonances.

However, for the real scenario considering Earth, we can see that both the variations of  $\Delta a$  and  $\Delta \lambda$  are constrained and oscillate with a longer period of  $\sim 40$  yr over time. This phenomenon can be understood as the motion of Kamo'oailewa being actually stably trapped near Earth owing to the quasi-satellite resonance, and the small perturbation of the Yarkovsky effect cannot destabilize this state. In fact, Kortenkamp (2013) showed that the orbit of interplanetary dust particles can be trapped in the 1:1 co-orbital resonance with Earth when the influence of the nongravitational effects, including the radiation pressure, Poynting–Robertson light drag, and solar wind drag, are considered. Here we show that the influence of the Yarkovsky effect can have a similar effect in the quasi-satellite regime.

To better understand the stability of Kamo'oailewa's orbit due to the Yarkovsky effect, a comparison of the variations of  $\Delta \lambda$  over 100 yr with five Earth quasi-satellites discovered so far, i.e., (164207) 2004 GU9, (277810) 2006 FV35, 2013 LX28, 2014 OL339, and 2023 FW13, is illustrated in the left panel of Figure 3, in which we find that only 2004 GU9 and 2023 FW13 show obvious oscillations similar to Kamo'oailewa, while the variation amplitude of Kamo'oailewa remains smallest. For the other three cases, however, they still exhibit remarkable drifts. The dynamical mechanism that caused this difference will be investigated in the future. This observation demonstrates that Kamo'oailewa's orbit is the most stable one in terms of the Yarkovsky perturbation among the six quasi-satellites.

It is noteworthy that this feature of Kamo'oailewa may hinder the Yarkovsky detection using ground-based astrometry, although the situation may be complicated since the detection S/N depends not only on orbital drift in the heliocentric frame but also on the observational conditions related to ground-based stations, such as the distance to the asteroid, the number of observations, the observational accuracy, etc. Nevertheless, to analyze this feature quantitatively, we carry out a series of orbital fitting including the Yarkovsky effect for the six quasi-satellites using simulated observations.

The values of  $A_2$  for all the asteroids are assumed to be  $-1.0 \times 10^{-13}$  au day $^{-2}$  in our simulations. In addition, the asteroids are observed from the geocentric framework, which can be a good approximation of a ground-based station owing to a small parallax (typically less than 1') relative to the asteroids. The observational accuracy of the station is assumed to be 0".3, and constraints from the limit magnitude, asteroid–Sun angle, and asteroid–Moon angle are not considered. The simulated astrometric observations are carried out on the brightest day of the year, with four observations made at 10-minute intervals for each batch of data. We fix the start observation time and vary only the end time for each case. The evolution of the Yarkovsky detection S/N over the observation time span between 3 and 100 yr is obtained from the orbital fit, as shown in the right panel of Figure 3, from which we can see

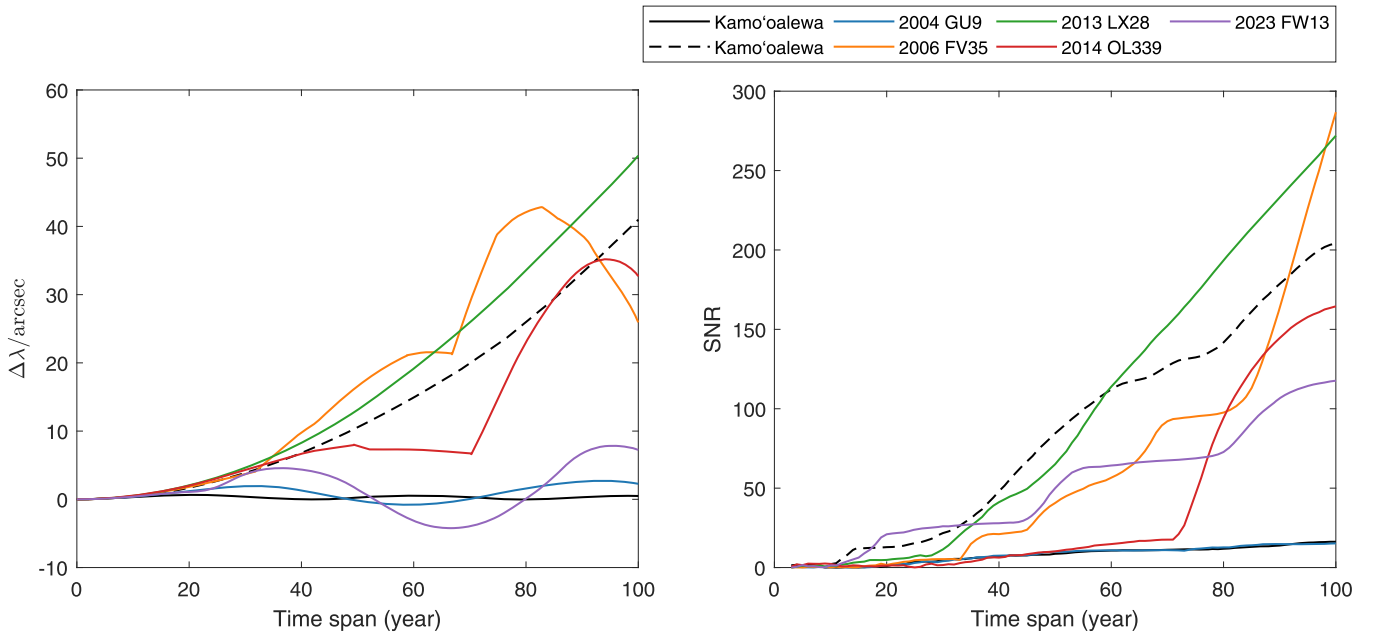


**Figure 3.** The left panel shows the variations of  $\Delta\lambda$  for the six Earth quasi-satellites over 100 yr with the same initial states. The right panel shows the evolution of the Yarkovsky detection S/N with different observational time spans with simulated optical astrometry for the quasi-satellites. The initial epochs are set to 1950 January 1 for 2013 LX28 and 2000 January 1 for the other five asteroids, to ensure that the 100 yr time spans are within the quasi-satellite periods. The black dashed lines denote those results for Kamo'oalewa without considering the gravity of Earth. Here  $A_2$  is assumed to be  $-1.0 \times 10^{-13}$  au day $^{-2}$ .

**Table 1**  
Yarkovsky-included Solutions and the  $1\sigma$  Uncertainties at 2023 February. 25 00:00:00 TDB in the J2000 Ecliptic System

Para.	This Work ( $S_7^*$ )	This Work ( $S_7$ )	Unit
Semimajor axis ( $a$ )	$1.001007386 \pm 1.5 \times 10^{-8}$	$1.001007397 \pm 1.6 \times 10^{-8}$	au
Eccentricity ( $e$ )	$0.102825645 \pm 3.9 \times 10^{-7}$	$0.102825664 \pm 3.9 \times 10^{-7}$	...
Inclination ( $i$ )	$7.79201870 \pm 2.7 \times 10^{-5}$	$7.79202059 \pm 2.7 \times 10^{-5}$	deg
Longitude of ascending node ( $\Omega$ )	$65.90561406 \pm 2.1 \times 10^{-5}$	$65.90561102 \pm 2.1 \times 10^{-5}$	deg
Argument of perihelion ( $\omega$ )	$305.35162823 \pm 2.6 \times 10^{-5}$	$305.35162629 \pm 2.6 \times 10^{-5}$	deg
Mean anomaly ( $M$ )	$141.14310070 \pm 3.6 \times 10^{-5}$	$141.14308147 \pm 3.7 \times 10^{-5}$	deg
Position ( $x$ )	$-150252517.8 \pm 35.6$	$-150252498.2 \pm 37.6$	km
Position ( $y$ )	$57277763.1 \pm 23.0$	$57277816.5 \pm 36.9$	km
Position ( $z$ )	$21969115.7 \pm 81.6$	$21969121.6 \pm 81.8$	km
Velocity ( $v_x$ )	$-11.2749657 \pm 4.6 \times 10^{-6}$	$-11.2749753 \pm 6.9 \times 10^{-6}$	km s $^{-1}$
Velocity ( $v_y$ )	$-24.9419584 \pm 1.1 \times 10^{-5}$	$-24.9419539 \pm 1.1 \times 10^{-5}$	km s $^{-1}$
Velocity ( $v_z$ )	$0.0150928 \pm 8.1 \times 10^{-7}$	$0.0150941 \pm 1.1 \times 10^{-6}$	km s $^{-1}$
$A_2$	$-1.470 \pm 0.400$	$-1.075 \pm 0.447$	$10^{-13}$ au day $^{-2}$
$\langle da/dt \rangle$	$-63.06 \pm 17.15$	$-46.10 \pm 19.18$	$10^{-4}$ au Myr $^{-1}$

**Note.** The orbital solutions are initially determined in the middle epoch of the observation arc and then propagated to near the current epoch.

that the S/N increases with time as expected. However, the change rate for Kamo'oalewa (as well as 2004 GU9) is much smaller than those of the other asteroids, which clearly demonstrates that the peculiar orbital characteristics of Kamo'oalewa lead to a reduced Yarkovsky detection S/N.

### 3.2. Results of Orbital Fit

Although we have demonstrated that the orbital drift induced by the Yarkovsky effect for Kamo'oalewa is alleviated by strong gravitational perturbation of Earth, it is still possible to obtain a valid Yarkovsky detection if the observations are qualified, as shown by the simulations in Figure 3. By implementing the latest debiasing technique of Eggl et al. (2020) in the open-source OrbFit 5.0.7 package (<http://adams.dm.unipi.it/orbfit/>; Consortium et al. 2011) and using the weighting scheme of Vereš et al. (2017), Liu et al. (2022)

derived  $A_2 = (-1.434 \pm 0.410) \times 10^{-13}$  au day $^{-2}$  for Kamo'oalewa, whose S/N is greater than the threshold of 3. Here we also conduct the seven-dimensional correction with the same observations with our SBORD package and detect  $A_2 = (-1.470 \pm 0.400) \times 10^{-13}$  au day $^{-2}$ , with a variation of less than 3% in the nominal value, as shown in Table 1 (where the solution is denoted as  $S_7^*$ ). The difference between two results is marginal, which may be caused by the implementation of the force models, the propagators and the settings in the convergence schemes involved, etc.

Among the observations, however, a pair of precoveries released by the Apache Point–Sloan Digital Sky Survey (SDSS) on 2004 March 17 should be carefully examined. These data significantly extend the observational arc length from  $\sim 11$  to  $\sim 18$  yr, which may give rise to an inordinate estimation on the Yarkovsky effect, as explained by Chesley

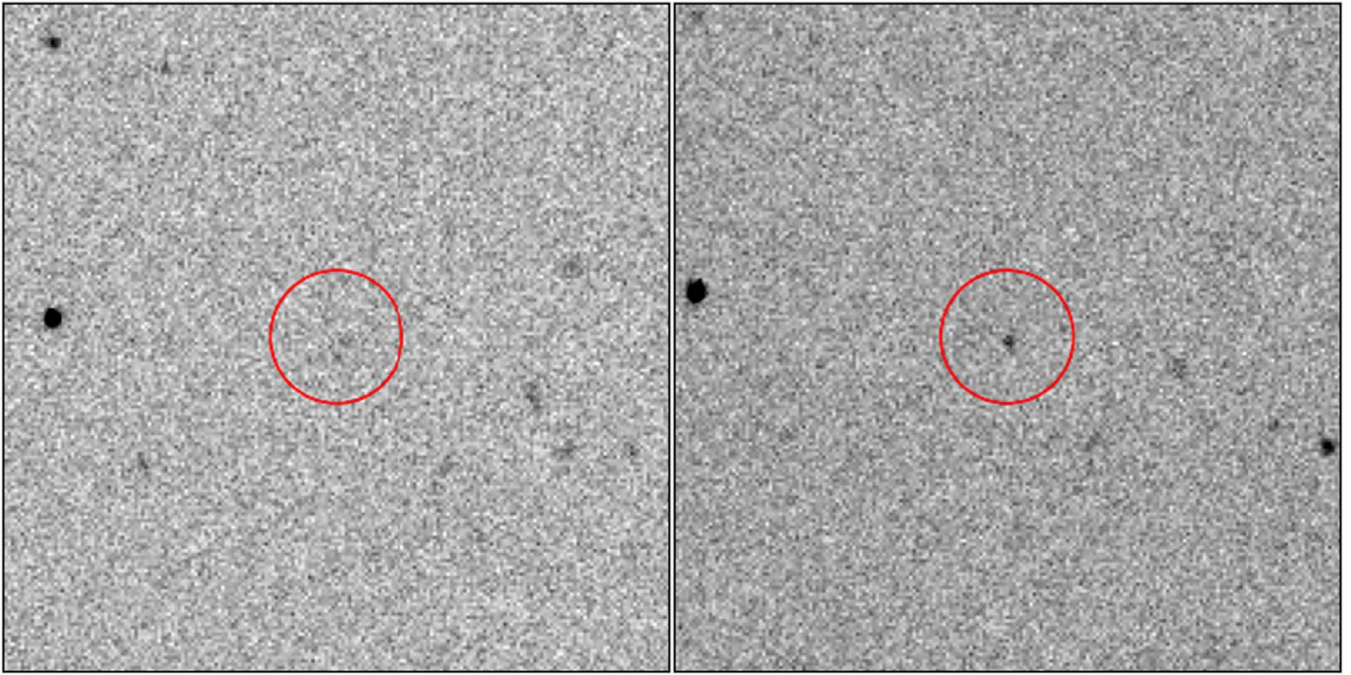


**Figure 4.** The two images of Kamo'oailewa (inside the red circles) observed by SDSS. The left was observed at 11:16:48.5 and the right at 11:21:35.1 UTC on 2004 March 17.

et al. (2016). Here we can obtain the two source images at the observation epochs from the SDSS archive server,<sup>4</sup> as shown in Figure 4. The inferred positions of Kamo'oailewa are circled in red, from which we can observe that the S/N of the left image may not be sufficient for precise targeting. The reason is that the apparent magnitude of Kamo'oailewa when observed by SDSS was  $\sim 22.8$ , which is close to the limit of the SDSS facility (Raymond et al. 2004). Since the astrometric quality depends significantly on the brightness of a target (Vereš et al. 2017) and a moving object has to be detected from at least two valid images, we propose to reject the data pair from the orbital fit out of a conservative rule.

Actually, we have two more points to support this treatment. First, we can perform the orbital fit using the data without the SDSS observations (the solution  $S_7$  in Table 1, as will be discussed in the following) and propagate the orbit to compute the R.A./decl. at the time of the SDSS observations. The resulting O-C is  $0''.23$  and  $0''.24$  for R.A. and  $-0''.78$  and  $-0''.97$  for decl., respectively. Although the predictions for R.A. are satisfactory, it is noteworthy that the differences in decl. reach up to 2.6 and 3.2 standard deviations (the weight for SDSS is  $0''.3$ ). Second, we need to use the star catalog flag (located in the 72nd character of the MPC 80-column observation) to estimate debiasing. However, the two SDSS observational data sets do not contain the flag information, making it impossible for us to conduct the debiasing, which increases the uncertainty of the observations. Anyhow, the rejection treatment will increase the orbital uncertainty estimate, but it is still worth considering, since having some margin in the ephemeris is usually a good idea for a space mission.

Under the consideration above on the data quality, the solution is recomputed and denoted as  $S_7$  in Table 1, which gives  $A_2 = (-1.075 \pm 0.447) \times 10^{-13}$  au day<sup>-2</sup>, or

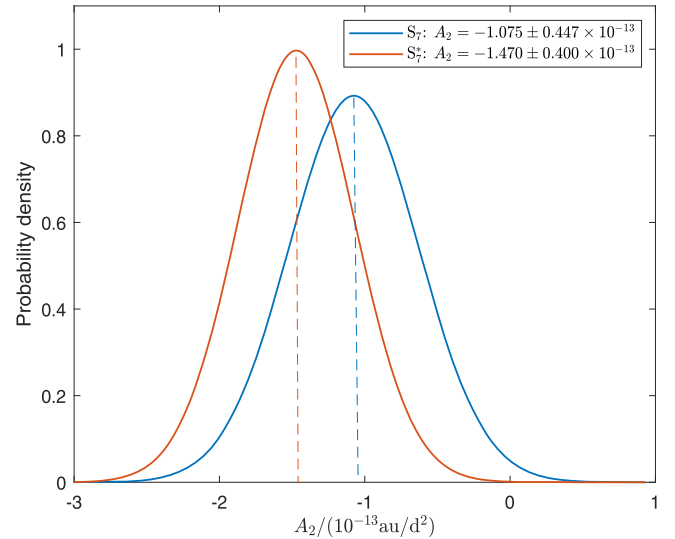


**Figure 5.** The probability density distributions of  $A_2$  for the solutions  $S_7$  and  $S_7^*$ .

equivalently  $\langle da/dt \rangle = (-46.10 \pm 19.18) \times 10^{-4}$  au Myr<sup>-1</sup>. The corresponding S/N is 2.4, slightly below the threshold of 2.5 for a weak detection. However, we conservatively accept this result as a weak detection, as the weights for the data are typically not that precise and a gravity-only solution may underestimate the orbital uncertainty if the Yarkovsky effect is ignored. Figure 5 shows the respective probability density distributions of  $A_2$  for the solutions  $S_7$  and  $S_7^*$ , from which we can see that  $S_7$  has a slightly lower estimate for the Yarkovsky drift than that of  $S_7^*$ , as well as a slightly larger uncertainty. Nevertheless, the result still indicates that  $A_2$  is likely negative, suggesting that Kamo'oailewa is probably a retrograde rotator, which is consistent with that of Liu et al. (2022).

<sup>4</sup> <https://dr12.sdss.org/>

**Table 2**  
Comparisons of Gravity-only Solutions with JPL Horizons at 2023 February 25 00:00:00 TDB in the J2000 Ecliptic System

Para.	JPL ( $S_6^J$ )	This Work ( $S_6$ )	This Work ( $S_6^*$ )	Unit
$a$	$1.001007435 \pm 3.5 \times 10^{-9}$	$1.001007435 \pm 2.8 \times 10^{-9}$	$1.001007441 \pm 2.1 \times 10^{-9}$	au
$e$	$0.102826447 \pm 2.4 \times 10^{-7}$	$0.102826443 \pm 2.1 \times 10^{-7}$	$0.102826990 \pm 1.2 \times 10^{-7}$	–
$i$	$7.79207609 \pm 1.7 \times 10^{-5}$	$7.79207538 \pm 1.4 \times 10^{-5}$	$7.79211288 \pm 8.3 \times 10^{-6}$	deg
$\Omega$	$65.90557126 \pm 1.5 \times 10^{-5}$	$65.90557112 \pm 1.3 \times 10^{-5}$	$65.90554701 \pm 1.0 \times 10^{-5}$	deg
$\omega$	$305.35166689 \pm 2.3 \times 10^{-5}$	$305.35166430 \pm 2.1 \times 10^{-5}$	$305.35169827 \pm 1.8 \times 10^{-5}$	deg
$M$	$141.14300832 \pm 2.3 \times 10^{-5}$	$141.14300950 \pm 2.1 \times 10^{-5}$	$141.14299347 \pm 2.1 \times 10^{-5}$	deg
$x$	$-150252552.0 \pm 35.2$	$-150252550.1 \pm 30.8$	$-150252628.9 \pm 18.7$	km
$y$	$57277879.8 \pm 26.2$	$57277885.1 \pm 23.2$	$57277827.2 \pm 14.7$	km
$z$	$21969289.4 \pm 51.1$	$21969287.4 \pm 43.3$	$21969400.6 \pm 25.0$	km
$v_x$	$-11.2749878 \pm 4.5 \times 10^{-6}$	$-11.2749886 \pm 4.0 \times 10^{-6}$	$-11.2749792 \pm 2.8 \times 10^{-6}$	km s <sup>-1</sup>
$v_y$	$-24.9419298 \pm 4.5 \times 10^{-6}$	$-24.9419295 \pm 3.7 \times 10^{-6}$	$-24.9419201 \pm 2.2 \times 10^{-6}$	km s <sup>-1</sup>
$v_z$	$0.0150945 \pm 1.2 \times 10^{-6}$	$0.0150946 \pm 1.0 \times 10^{-6}$	$0.0150925 \pm 8.0 \times 10^{-7}$	km s <sup>-1</sup>

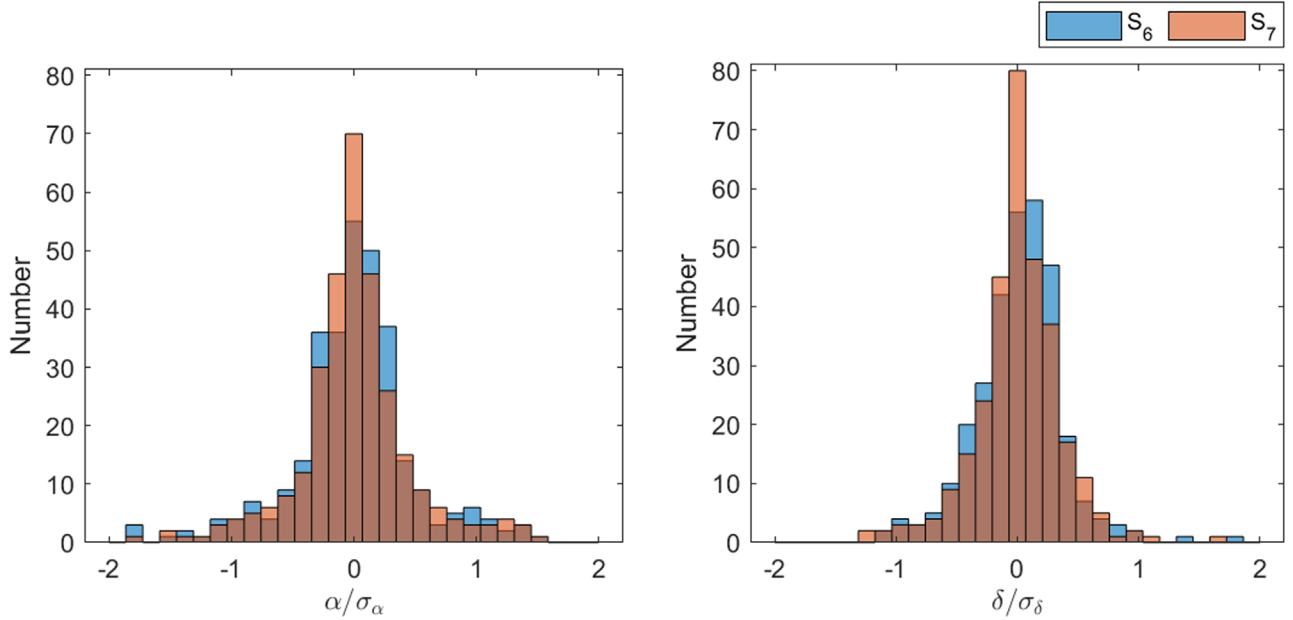


**Figure 6.** Histograms of normalized O–C residuals of R.A. ( $\alpha$ ) and decl. ( $\delta$ ) for the solutions  $S_6$  and  $S_7$ .

Note that the JPL Horizons online ephemeris system only presents a gravity-only solution (with a six-dimensional fit) for Kamo‘oalewa ( $S_6^J$ ), which is listed in Table 2. Using the above conservative rejection scheme, we can also compute a gravity-only solution, which is displayed in Table 2 ( $S_6$ ). Note that the difference in the nominal position between  $S_6^J$  and  $S_6$  is only  $\sim 6$  km, much smaller than the  $1\sigma$  uncertainty. However, if the SDSS data are included, the solution (denoted as  $S_6^*$ ) has a much larger positional difference of  $\sim 145$  km with  $S_6^J$ . These comparisons imply that the JPL solution may have de-weighted the SDSS data, which lends support to our conservative consideration on the data quality to some extent.<sup>5</sup>

Figure 6 presents the histograms of normalized O–C residuals for the solution  $S_6$  and  $S_7$ , from which we note that the distributions of the residuals are more concentrated around the zero-point when the Yarkovsky effect is introduced. In fact, the normalized  $\chi^2$  is 0.38752 and 0.36985 for  $S_6$  and  $S_7$ , respectively. Therefore, the latter is a better fit. In the following

<sup>5</sup> We note that the estimated uncertainties for the JPL solution are slightly larger than ours (the reason is unknown). However, these differences are not significant given the uncertainty in the accuracy of the observations.

discussions we will analyze the orbital uncertainty based on the solution  $S_7$ .

## 4. Analysis of Orbital Uncertainty

### 4.1. Orbital Uncertainty in Different Frames

The orbital uncertainty at the initial epoch  $t_0$  can be obtained from the covariance matrix  $P(t_0)$ , which is solved together with the orbit determination procedure. According to the linear covariance propagation theory, the covariance matrix  $P(t)$  at time  $t$  is given by

$$\begin{cases} P(t) = \Phi(t, t_0)P(t_0)\Phi(t, t_0)^T \\ \Phi(t, t_0) = \frac{\partial X(t)}{\partial X(t_0)} \end{cases}, \quad (4)$$

in which  $X$  is the seven-dimensional vector  $X = [Z, A_2]$  ( $Z$  represents the orbital parameters, which can be the Cartesian positions and velocities or the orbital elements).  $\Phi(t, t_0)$  is the  $7 \times 7$  state transition matrix (STM) that is derived numerically by integrating the variational equations (Montenbruck et al. 2002; Milani & Gronchi 2010). If the Cartesian coordinates are used, we can transform the covariance matrix  $P(t)$  to another

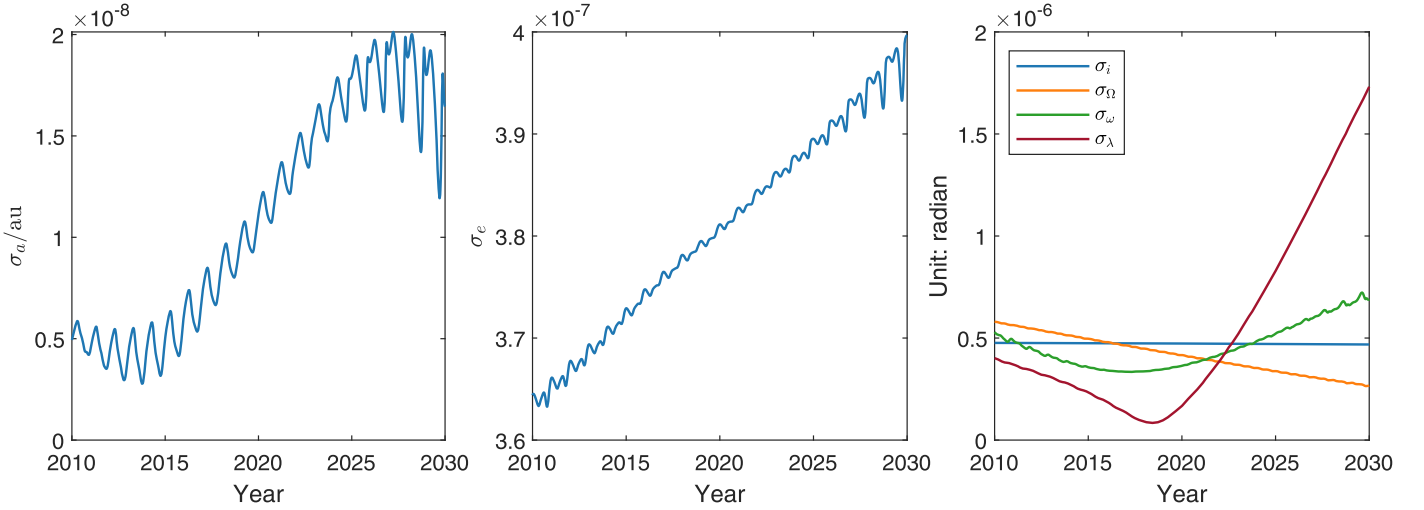


Figure 7. Time evolution of uncertainty in the orbital elements from 2010 to 2030 for the solution  $S_7$ .

reference system by

$$P'(t) = B \cdot P(t)B^T, \quad (5)$$

in which  $P'(t)$  is the covariance in the new reference and  $B$  is the rotation matrix between the two references. Note that the covariance remains unchanged if we apply a translation to an inertial frame.

Figure 7 shows the time evolution of the uncertainty in the orbital elements from 2010 to 2030 for our solution  $S_7$ , from which we can see that  $\sigma_a$ ,  $\sigma_e$ , and  $\sigma_i$  are relatively smaller compared to the results of the other angular elements  $\sigma_\Omega$ ,  $\sigma_\omega$ , and  $\sigma_\lambda$ , and  $\sigma_\lambda$  is generally the maximum one among the six. We find that  $\sigma_\lambda$  reaches a minimum value in  $\sim 2018$  and then gradually increases superlinearly with time, which is attributed to the uncertainty in the Yarkovsky effect.

In addition, Figure 8 shows the time evolution of the positional uncertainty ( $1\sigma$ ) for Kamo‘oalewa. The results in the four panels are the uncertainty of the Cartesian coordinates in the heliocentric frame, the RTN uncertainty in the heliocentric frame, the RTN uncertainty in the geocentric frame, and the Cartesian uncertainty in the geocentric rotating frame, respectively. We can see that all the results exhibit complicated cyclic changes with time, except that the uncertainty from 2010 to 2020 is generally smaller than that from 2020 to 2030, which can be explained by the fact that the orbit is constrained by the astrometry from 2010 to 2019 (the constraint by the observations in 2021 is weak owing to a relatively lower accuracy estimation).

According to the results in the two middle panels, we can see that the uncertainty from 2010 to 2020 is mainly concentrated along the radial direction of the orbit in the geocentric frame. This is because ground-based optical astrometry can provide a better constraint on the orbit along the geocentric transverse and normal directions, while the constraint for the radial direction is weaker. However, the uncertainty from 2020 to 2030 is more suitable for description in the heliocentric frame, where the transverse uncertainty gradually increases to a maximum of  $\sim 370$  km in 2030 while the radial and normal components remain within  $\sim 80$  km.

Moreover, monthly dependencies in the uncertainty can be observed from the oscillations in Figure 8. To better illustrate this phenomenon, Figure 9 shows the evolution in the

heliocentric RTN directions, with the month as the horizontal axis. The results clearly demonstrate the oscillations of the uncertainties within a year. However, due to the complicated orbital evolution relative to Earth, the month at the maximum amplitude shifts slowly with the year. For the period 2025–2027, which is more important for the mission, the uncertainty reaches a minimum in around January and a maximum in around July. As seen in the top right panel of Figure 1, the orbit of Kamo‘oalewa moves approximately toward the leading and trailing edges in January and July, respectively. The normal component always reaches a minimum around late May (or early June) or mid-November, which occurs when the orbit is moving around the ascending/descending nodes, or crossing the ecliptic.

#### 4.2. Uncertainty Propagation in the Quasi-satellite Regime

The previous subsection only analyzes the uncertainty propagation for a few years. However, due to the peculiar orbital configuration of Kamo‘oalewa, it will be helpful to improve the knowledge of the orbit propagation by investigating the uncertainty in the quasi-satellite regime for a longer period of time.

From Equation (4), the covariance matrix depends strongly on the STM, which is solved together with the orbit propagation. Similar to the study in Section 2.4, here we consider two force models to compute the STM in addition to the Yarkovsky force, where one takes into account the full planetary gravitational perturbations and the other includes those except Earth. Figure 10 shows the uncertainties of the semimajor axis, eccentricity, inclination, and mean longitude, respectively, for the two models, in which the initial covariances are taken from the solution  $S_7$ . The time range is from 2000 to 2200, well within the quasi-satellite period.

The results demonstrate that the along-track uncertainty  $\sigma_\lambda$  is undoubtedly the most significant component for both models. However, the evolution differs significantly between them: for the full model,  $\sigma_\lambda$  undergoes complex oscillatory changes with increasing amplitudes over time, while for the model without Earth the values increase quadratically at much faster rates. The difference in  $\sigma_\lambda$  between both can be as large as 40 times in 2200.



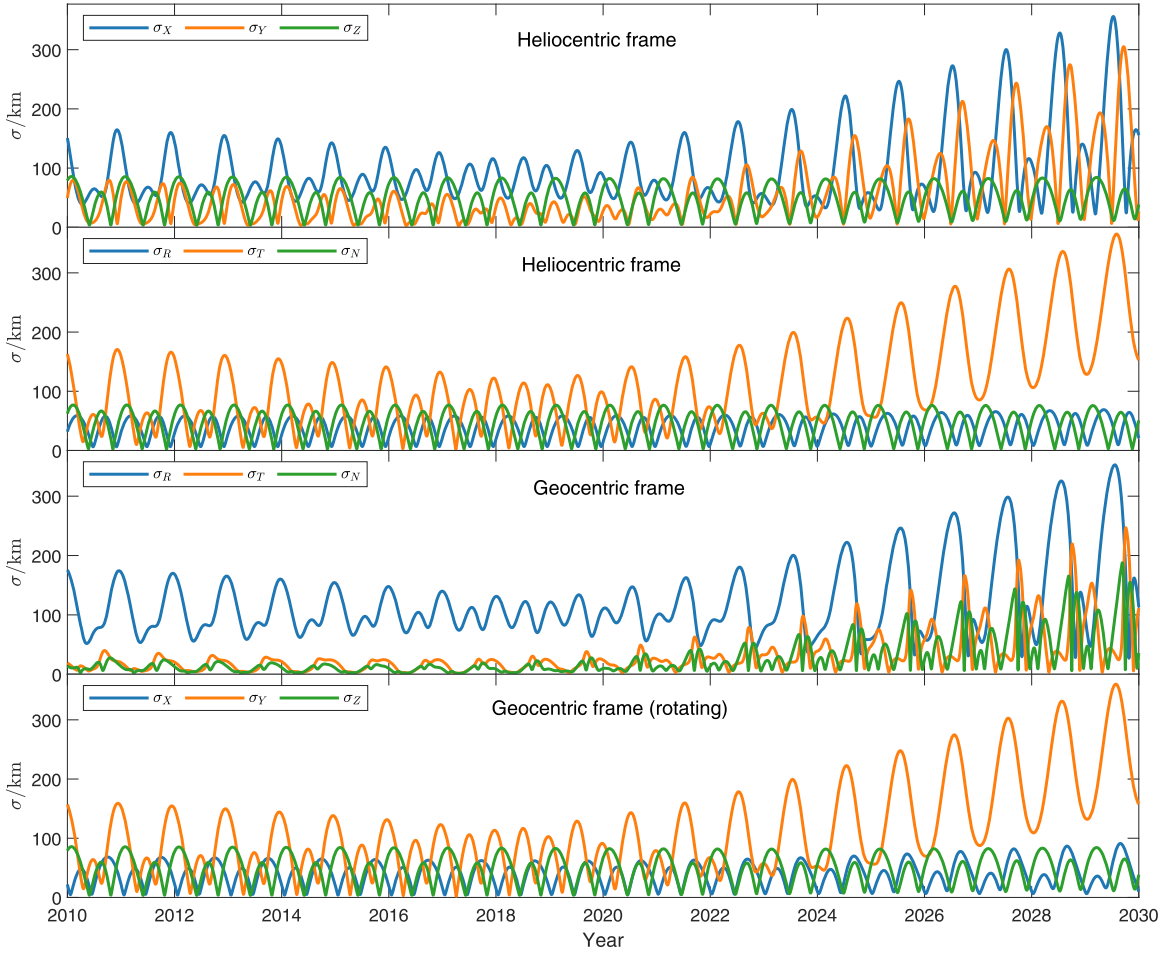


**Figure 8.** Variations of the positional uncertainty from 2010 to 2030 for the solution  $S_7$  in different frames. The top two panels show the changes in the heliocentric frame for the Cartesian and RTN coordinates, respectively. The third panel shows the results for the RTN directions in the geocentric frame, and the bottom panel shows the results for the Cartesian coordinates in the geocentric Sun–Earth rotating frame.

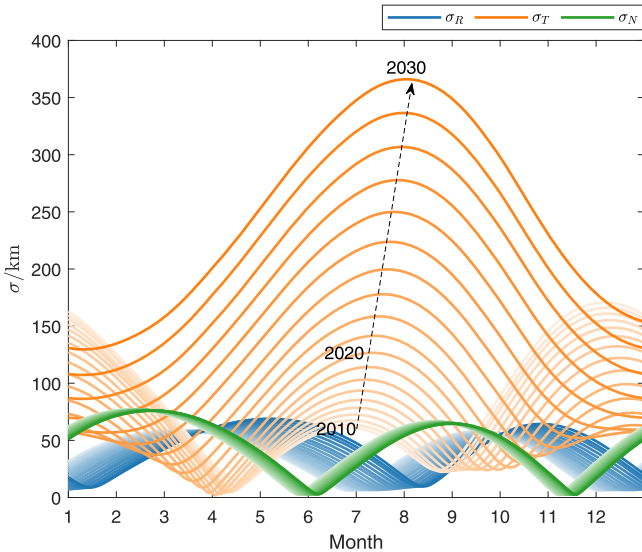


**Figure 9.** Plots of the positional uncertainties for the solution  $S_7$  from 2010 to 2030 in the heliocentric RTN directions, in which the horizontal axis is taken as the month and the color gradient from dark to light indicates the evolution of the year. The dashed line arrow shows the evolution direction for  $\sigma_T$ .

The propagation of  $\sigma_\lambda$  is mainly governed by the terms  $\frac{\partial \lambda(t)}{\partial a_0}$  and  $\frac{\partial \lambda(t)}{\partial A_2}$  in the STM, which correspond to the uncertainties in

the initial semimajor axis and the Yarkovsky effect, respectively. Figure 11 shows the time evolution of the two partial derivatives for the two models. We find that the magnitudes of the variations in  $\frac{\partial \lambda(t)}{\partial A_2}$  are significantly larger than that of  $\frac{\partial \lambda(t)}{\partial a_0}$  for both models, indicating that the uncertainty caused by the Yarkovsky effect is much larger than that of the uncertainty in the initial semimajor axis for this propagation of 200 yr. Therefore, we will focus on the evolution of  $\frac{\partial \lambda(t)}{\partial A_2}$  in the following.

As expected, for the model without Earth,  $\frac{\partial \lambda(t)}{\partial A_2}$  propagates quadratically with time. For the full model, however, the evolution oscillates over a period of about 40 yr, with the amplitude increasing slowly with time. This very different mode of change explains the remarkable difference in the evolution of  $\sigma_\lambda$ . Note that Kamo‘oalewa would not behave as a quasi-satellite when the perturbation of Earth is excluded. This phenomenon indicates that the propagation of the orbital uncertainty under the Yarkovsky effect is strongly constrained, which facilitates the orbital prediction throughout the quasi-satellite period.

To understand the oscillatory variation in  $\sigma_\lambda$  for the full model, we use the following forward difference method to

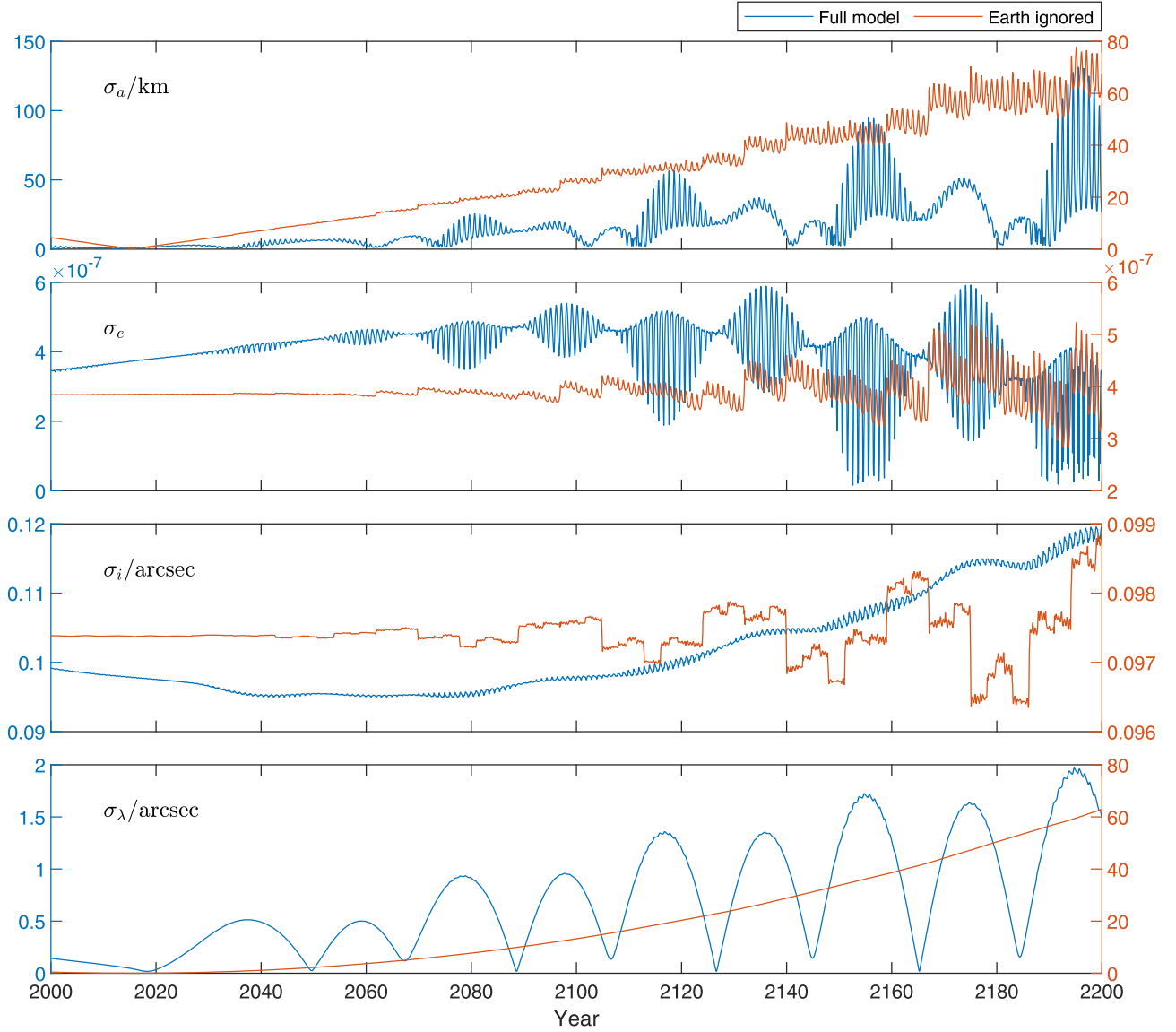


**Figure 10.** The panels show the uncertainty in the semimajor axis, eccentricity, inclination, and mean longitude, respectively, from 2000 to 2200. The results in blue are computed using the full planetary gravitational perturbation model, and the red ones exclude the Earth perturbation.

approximately calculate the partial derivative:

$$\frac{\partial \lambda(t)}{\partial A_2} \approx \frac{\lambda(Z, A_2 + h) - \lambda(Z, A_2)}{h}, \quad (6)$$

in which  $h$  is a small quantity. Since  $A_2$  is also very small, we can safely substitute  $h$  with  $-A_2$ , and then we have

$$\frac{\partial \lambda(t)}{\partial A_2} \approx \frac{\lambda(Z, 0) - \lambda(Z, A_2)}{-A_2} = \frac{\Delta \lambda}{A_2}, \quad (7)$$

in which  $\Delta \lambda$  is the difference in the mean longitude between the Yarkovsky-included and gravity-only model, a typical example of which can be seen in Figure 2. This feature indicates that the evolution of the along-track uncertainty  $\sigma_\lambda$  under the influence of the Yarkovsky effect is consistent with the evolution of  $\Delta \lambda$ , which is governed by the quasi-satellite resonance with Earth, as explained in Section 3.1.

## 5. Summary and Conclusions

469219 Kamo'oalewa is a small near-Earth asteroid, which is currently known as the most stable quasi-satellite of Earth. In addition, this asteroid is the sample-return target of the Chinese Tianwen-2 mission scheduled for launch in 2025. To facilitate the mission, precise orbit determination is important to ensure a successful rendezvous with the object. However, the small size of Kamo'oalewa may correspond to a remarkable Yarkovsky acceleration. This is usually the most important nongravitational force that can affect the orbital precision and may be detected from the orbital fit. Considering that additional observations may not be available prior to the launch (the apparent magnitude of the observation window at the brightest time is dimming in the next few years), the uncertainty estimate for the next few years including the Yarkovsky effect is needed. In addition, due to the peculiar quasi-satellite orbit, the uncertainty characteristics in the quasi-satellite regime are analyzed, which provides more insights into the orbit propagation of Kamo'oalewa.

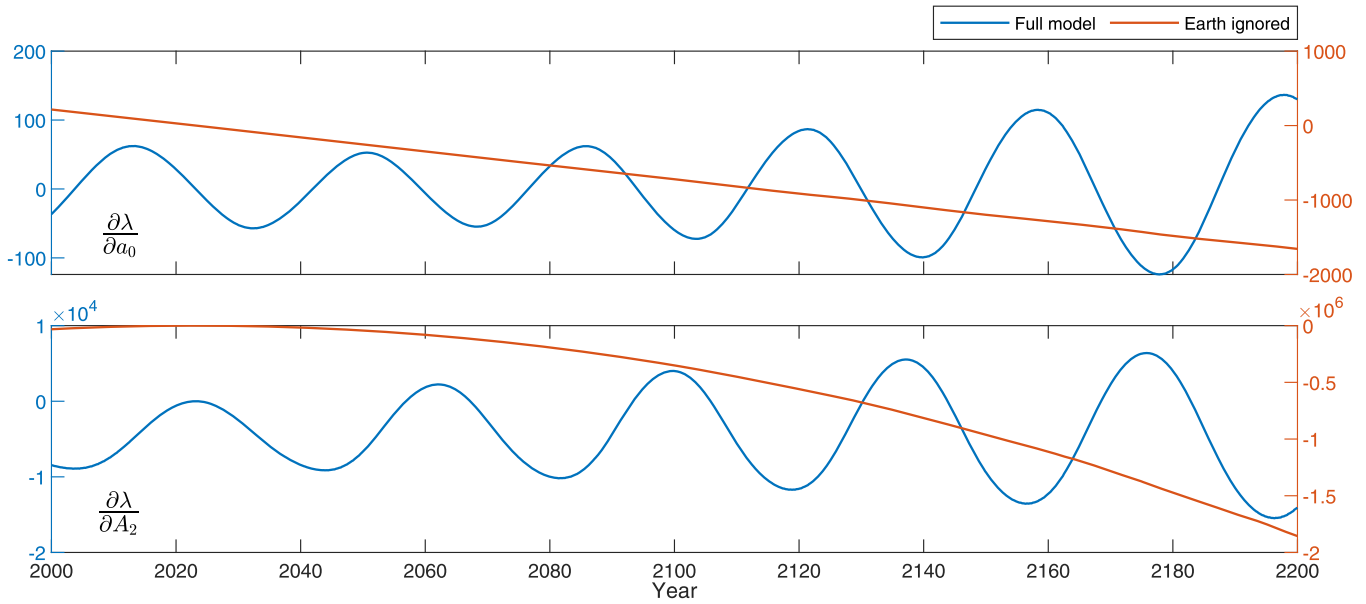


**Figure 11.** The time evolution of  $\frac{\partial \lambda(t)}{\partial a_0}$  and  $\frac{\partial \lambda(t)}{\partial A_2}$  for the two force models from 2000 to 2200, in which the initial epoch is 2023 February 25 00:00:00 TDB.

In this work, we first show numerically that the Yarkovsky effect can cause a periodic change in Kamo‘oalewa’s semimajor axis owing to its particular quasi-satellite resonance with Earth, rather than a normal secular drift for a general asteroid. This feature can reduce the sensitivity of the orbital drift to the influence of the Yarkovsky effect, to some extent making it more difficult to detect the drift from the orbital fitting, as demonstrated by the comparisons of S/N over observational arc among the six Earth quasi-satellites discovered so far (Figure 3).

Nevertheless, we still find a weak detection of the Yarkovsky effect using the ground-based optical observations spanning from 2011 to 2021 (the precoveries by SDSS in 2004 are rejected owing to the poor quality), giving  $A_2 = (-1.075 \pm 0.447) \times 10^{-13} \text{ au day}^{-2}$ , with a slightly lower significance in the detection S/N than that of Liu et al. (2022). Here we take a relatively conservative approach and reject a pair of pre-recovery SDSS observations to avoid overestimating the drift, which is supported by the possible lower S/N in one of the source images.

Based on our derived solution including the Yarkovsky effect, the orbital uncertainty propagation of Kamo‘oalewa is extensively studied. We find that the positional uncertainty comes mainly from the radial direction for the geocentric orbit in 2010–2020 and is concentrated in the transverse direction for the heliocentric orbit in 2020–2030. The variation of the uncertainty within a year is clearly related to the month owing to the peculiar orbit configuration. The heliocentric transverse uncertainty is minimized around January and maximized around July in 2025–2027, corresponding to the period when the orbit moves toward the leading and trailing edges, respectively.

Finally, we further investigate a long-term uncertainty propagation in the quasi-satellite regime. We show that the along-track uncertainty with the Yarkovsky effect can be significantly constrained during this period, rather than a general rapid quadratic propagation. This feature indicates that the orbit precision of this asteroid is relatively stable even when the uncertainty of the Yarkovsky effect is considered.

Note that the above conclusions about the orbital uncertainty in the next few years are based on the ground-based optical observations from 2011 to 2021. Since the T12 station accounts for most of the observations, the treatment of the weighting will lead to a various solution. In particular, since the uncertainties have been inflated by a  $\sqrt{N}$  factor to mitigate possible effects of unresolved systematics (Vereš et al. 2017), this artificial treatment will also add more uncertainties in the weight and then finally affect the solution. With the addition of spacecraft-based radio and optical observations during the rendezvous, the uncertainty in the Yarkovsky detection and orbital precision is likely to be significantly improved.

Nevertheless, the uncertainty analysis procedures proposed here remain valid. Moreover, since the behavior of orbital variations under the influence of the Yarkovsky effect is an intrinsic orbital property of Kamo‘oalewa, the uncertainty propagation for a longer period of time in the quasi-satellite regime is still constrained, and even the orbital solution would be improved in the future. This feature may also apply to other quasi-satellites (e.g., 2004 GU9 and 2023 FW13), which will be explored in a forthcoming study.

### Acknowledgments

We thank the referee for constructive comments and suggestions to improve the manuscript. This work is financially supported by the B-type Strategic Priority Program of the Chinese Academy of Sciences (grant No. XDB41000000), the National Natural Science Foundation of China (grant Nos. 11873098, 12150009, 12033010, 62227901, 12073084), the Natural Science Foundation for Young Scientists of Jiangsu Province (grant No. BK20221162), the Space Debris and Near-Earth Asteroid Defense Research Project (grant Nos. KJSP2020020204 and KJSP2020020102), and the Foundation of Minor Planets of the Purple Mountain Observatory. We appreciate Yi Xie and Steven R. Chesley for their insightful discussions.

## ORCID iDs

Shoucun Hu  <https://orcid.org/0000-0003-2304-3575>  
 Haoxuan Jiang  <https://orcid.org/0000-0003-4067-3616>  
 Jianghui Ji  <https://orcid.org/0000-0002-9260-1537>

## References

- Botke, W., Vokrouhlický, D., Rubincam, D. P., & Broz, M. 2002, *Asteroids III*, Vol. 395 (Tucson, AZ: Univ. Arizona Press), 408
- Botke, W. F., Jr., Vokrouhlický, D., Rubincam, D. P., & Nesvorný, D. 2006, *AREPS*, **34**, 157
- Chesley, S. R., Farnocchia, D., Nolan, M. C., et al. 2014, *Icar*, **235**, 5
- Chesley, S. R., Farnocchia, D., Pravec, P., & Vokrouhlický, D. 2016, in IAU Symp. 318, *Asteroids: New Observations, New Models* (Cambridge: Cambridge Univ. Press), 250
- Chesley, S. R., Ostro, S. J., Vokrouhlický, D., et al. 2003, *Sci*, **302**, 1739
- Chi, Z., Li, H., Jiang, F., & Li, J. 2018, *Ap&SS*, **363**, 1
- Connors, M., Chodas, P., Mikkola, S., et al. 2002, *M&PS*, **37**, 1435
- Orbfit Consortium, et al. 2011, *OrbFit: Software to Determine Orbits of Asteroids*, Astrophysics Source Code Library, ascl:1106.015
- De la Fuente Marcos, C., & De la Fuente Marcos, R. 2016, *MNRAS*, **462**, 3441
- Del Vigna, A., Faggioli, L., Milani, A., et al. 2018, *A&A*, **617**, A61
- Deo, S. N., & Kushvah, B. S. 2017, *A&C*, **20**, 97
- Desmars, J. 2015, *A&A*, **575**, A53
- Dziadura, K., Oszkiewicz, D., & Bartczak, P. 2022, *Icar*, **383**, 115040
- Eggl, S., Farnocchia, D., Chamberlin, A. B., & Chesley, S. R. 2020, *Icar*, **339**, 113596
- Farinella, P., Vokrouhlický, D., & Hartmann, W. K. 1998, *Icar*, **132**, 378
- Farnocchia, D., Chesley, S., Vokrouhlický, D., et al. 2013, *Icar*, **224**, 1
- Fehlberg, E. 1969, *Compu*, **4**, 93
- Fenucci, M., & Novaković, B. 2021, *AJ*, **162**, 227
- Fenucci, M., Novaković, B., Vokrouhlický, D., & Weryk, R. J. 2021, *A&A*, **647**, A61
- Greenberg, A. H., Margot, J. L., Verma, A. K., et al. 2017, *AJ*, **153**, 108
- Greenberg, A. H., Margot, J. L., Verma, A. K., Taylor, P. A., & Hodge, S. E. 2020, *AJ*, **159**, 92
- Hanuš, J., Vokrouhlický, D., Delbo, M., et al. 2018, *A&A*, **620**, L8
- Heiligers, J., Fernandez, J. M., Stohman, O. R., & Wilkie, W. K. 2019, *AsDyn*, **3**, 231
- Hu, S., Richardson, D. C., Zhang, Y., & Ji, J. 2021, *MNRAS*, **502**, 5277
- Huang, J., Ji, J., Ye, P., et al. 2013, *NatSR*, **3**, 3411
- Huang, J., Zhang, X., Wang, T., et al. 2020, EPSC, EPSC2020–1126
- Jiang, H., Yu, L., & Ji, J. 2019, *AJ*, **158**, 205
- Jin, W., Li, F., Yan, J., et al. 2020, *MNRAS*, **493**, 4012
- Kortenkamp, S. J. 2013, *Icar*, **226**, 1550
- Li, X., & Scheeres, D. J. 2021, *Icar*, **357**, 114249
- Liu, L., Yan, J., Ye, M., et al. 2022, *A&A*, **667**, A150
- Milani, A., & Gronchi, G. 2010, *Theory of Orbit Determination* (Cambridge: Cambridge Univ. Press)
- Montenbruck, O., Gill, E., & Lutze, F. 2002, *ApMRv*, **55**, B27
- Morais, M., & Morbidelli, A. 2002, *Icar*, **160**, 1
- Morbidelli, A., & Vokrouhlický, D. 2003, *Icar*, **163**, 120
- Namouni, F. 1999, *Icar*, **137**, 293
- Nugent, C., Margot, J., Chesley, S., & Vokrouhlický, S. 2012, *AJ*, **144**, 60
- Park, R. S., Folkner, W. M., Williams, J. G., & Boggs, D. H. 2021, *AJ*, **161**, 105
- Pousse, A., Robutel, P., & Vienne, A. 2017, *CeMDA*, **128**, 383
- Pravec, P., & Harris, A. W. 2000, *Icar*, **148**, 12
- Qi, Y., & Qiao, D. 2022, *AsDyn*, 2022, 1
- Raymond, S. N., Mikkola, G., Fraser, O. J., et al. 2004, *AJ*, **127**, 2978
- Rozitis, B., Duddy, S. R., Green, S. F., & Lowry, S. C. 2013, *A&A*, **555**, A20
- Rozitis, B., & Green, S. F. 2011, *MNRAS*, **415**, 2042
- Rozitis, B., & Green, S. F. 2014, *A&A*, **568**, A43
- Sharkey, B. N., Reddy, V., Malhotra, R., et al. 2021, *ComEE*, **2**, 1
- Sidorenko, V. V., Neishtadt, A. I., Artemyev, A. V., & Zelenyi, L. M. 2014, *CeMDA*, **120**, 131
- Tholen, D. J., Ramanjooloo, Y., Fohring, D., Hung, D., & Micheli, M. 2016, *AAS Meeting Abstracts*, **48**, 311
- Venigalla, C., Baresi, N., Aziz, J. D., et al. 2019, *JSpRo*, **56**, 1121
- Vereš, P., Farnocchia, D., Chesley, S. R., & Chamberlin, A. B. 2017, *Icar*, **296**, 139
- Vokrouhlický, D. 1999, *A&A*, **344**, 362
- Vokrouhlický, D., Milani, A., & Chesley, S. 2000, *Icar*, **148**, 118
- Winter, O., Sfair, R., Moraes, R., Gomes, L., & Borderes Motta, G. 2022, in 44th COSPAR Scientific Assembly, Vol. 44 (Athens: COSPAR), 274
- Yan, J., Liu, L., Ye, M., et al. 2022, *Icar*, 2022, 115120
- Zhang, T., Xu, K., & Ding, X. 2021a, *NatAs*, **5**, 730
- Zhang, X., Luo, Y., Xiao, Y., et al. 2021b, *SpScT*, 2021, 1